Evaluating advection/transport schemes using interrelated tracers, scatter plots and numerical mixing diagnostics

P. H. Lauritzen[a*] and J. Thuburn[b]

[a]*Climate and Global Dynamics Division, National Center for Atmospheric Research*[†], *Boulder, USA*
[b]*College of Engineering, Mathematics and Physical Sciences, University of Exeter, Exeter, UK*
[*]Correspondence to: National Center for Atmospheric Research, 3090 Center Green Drive, Boulder CO 80301, USA
E-mail: pel@ucar.edu

Atmospheric tracers are often observed to be functionally related, and these relations can be physically or chemically significant. It is therefore highly desirable that the transport schemes used in chemistry and chemistry-climate models should not disrupt such functional relations in unphysical ways through numerical mixing or, indeed, unmixing. Here, diagnostics are proposed that quantify numerical mixing by a transport scheme for a single tracer, two tracers that are nonlinearly related, and three (or more) tracers that add up to a constant. For the two-tracer test the question of how physically reasonable the numerical mixing is can be addressed by using scatter/correlation plots. Truncation errors will, in general, result in scatter points deviating from the preexisting functional curve and thereby introduce numerical mixing between the tracers. The proposed diagnostics quantify the mixing in terms of the normalized distances between the preexisting functional curve and scatter points, and divide it into three categories: real mixing and two types of spurious numerical unmixing. For the three-tracer test we quantify, in terms of standard error norms, how nearly a transport scheme can preserve the sum by transporting the individual tracers.

The mixing diagnostics do not require the knowledge of the analytical solution to the transport problem for the individual tracers. However, using an idealized flow field and spatial distributions facilitates the use of the mixing diagnostics in transport scheme development. Hence we propose to exercise the new mixing diagnostics using an idealized but highly deformational analytical flow field. Example results using the CSLAM (Conservative Semi-LAgrangian Multi-tracer) scheme are presented. Copyright © 2011 Royal Meteorological Society

1. Introduction

Tracers (chemical species, aerosols, different forms of water in the atmosphere, etc.) are often observed to be related through functional relations. Perhaps the most striking

example of interrelated tracers in the atmosphere is long-lived species in the lower stratosphere such as NO_y and N_2O (for a recent review see, e.g., Plumb 2007). When the mixing ratios of N_2O and NO_y are plotted against each other to form a scatter (or correlation) plot, the scatter points collapse to a remarkably compact curve despite the wide range in spatial scale (from a few to several thousand kilometers). Such compact scatter plots can be physically or chemically significant; for example, departures from

[†]The National Center for Atmospheric Research is sponsored by the National Science Foundation.

compactness have been used to quantify chemical ozone loss in the ozone hole (Proffitt *et al.* 1990). It is therefore highly desirable that transport schemes used in modelling the atmosphere should respect such functional relations and not disrupt them in physically unrealistic ways.

Similarly, the total of chemical species within some chemical family may be preserved following an air parcel although the individual species have a complicated relation to each other and may be transformed into each other through chemical reactions. For example, total chlorine consists of several organic and inorganic species; however, the mixing ratio of total chlorine in a stratospheric air parcel can not exceed the value determined by surface sources and is approximately preserved on short time-scales. The total chlorine thus provides an important constraint on the chemistry. Similar arguments can be made for aerosol-cloud interactions (Ovtchinnikov and Easter 2009) where important physical properties are derived from several tracers. The issue that may arise in this context is that when models transport individual tracers with a *shape-preserving* scheme, there is in general no guarantee that the sum of the tracers (or any other function that is a function of more than two tracers) is shape-preserving, and therefore the sum may contain unphysical values.

For Eulerian transport schemes—those that solve the governing equations on a fixed grid—truncation errors inevitably lead to some *numerical mixing*. In the free atmosphere the numerical mixing is typically much stronger than the mixing due to physical atmospheric processes (Thuburn and Tan 1997; Balluch and Haynes 1997) and is related to the grid resolution. Transport schemes can also produce numerical unmixing, that is, up-gradient transport, for example through dispersion errors. Because strong unmixing is highly undesirable, practical transport schemes are usually configured so that unmixing is weak, for example through the inclusion of flux limiters or additional diffusion; nevertheless, unmixing can be completely eliminated only by the use of a monotone scheme, which can be at best first-order accurate (see section 2), so a certain amount of unmixing is typically tolerated in practice.

These mixing and unmixing issues become especially relevant when two or more tracers are involved. As alluded to above, tracers are usually transported separately although they may be related through functional relations. Truncation errors may perturb preexisting functional relations between tracers (Thuburn and McIntyre 1997, hereafter referred to as TM97) and cause unphysical values in derived quantities (Ovtchinnikov and Easter 2009). For pairs of tracers that are linearly related, a linear transport scheme will preserve that linear relation but, for higher than first-order schemes, will not be shape-preserving. There does exist a fairly wide class of transport schemes (Lin and Rood 1996, TM97—TM97 call them *semi-linear*) that are shape-preserving on individual tracers and preserve linear relations between pairs of tracers. However, they will not, in general, preserve nonlinear relations between tracers. Distortion of preexisting functional relations between tracers can be interpreted as numerical mixing or numerical spreading. Careful analysis of numerical mixing can provide insight into how physically realistic the numerical mixing introduced by the transport operator is (TM97); in other words, does the mixing resemble 'physical' mixing as observed in the atmosphere (here referred to as *real mixing*) or is it producing spurious unmixing. Real mixing between two air parcels can only create new scatter points that lie on mixing lines, i.e. straight lines connecting the two scatter points corresponding to the original parcels. Hence, real mixing between two nonlinearly correlated tracers can only produce new data points on the scatter plot that are inside the *convex hull* of the original data, since these are the only points that can be built up by combinations of mixing lines. Any new scatter point outside the convex hull must be a result of numerical unmixing.

Ovtchinnikov and Easter (2009) considered three tracers whose sum was initially constant. They demonstrated how numerical errors introduced by transporting the three tracers separately distorted the sum (a derived quantity). We are not aware of any transport scheme that is both shape-preserving on individual tracers and sum-preserving for three or more tracers, and, indeed, it is not clear whether such a scheme is possible.

Despite the importance of preserving or not spuriously distorting relationships between tracers, as discussed above, idealized testing of transport schemes usually only takes place in a single tracer setup (for an overview see, e.g., Lauritzen *et al.* 2011). That is, for some analytical flow field where the analytical solution is known, some distribution is transported as an inert and passive scalar and thereafter conventional/standard error norms, such as ℓ_1, ℓ_2, and ℓ_∞ (see Appendix A), are computed. While such error norms are indeed useful to quantify the numerical errors for a single tracer, it is not necessarily straightforward to deduce how preexisting functional relations between tracers are altered by truncation errors.

As far as the authors are aware the only exceptions to the widely used single tracer testing methodology in atmospheric transport scheme development, are the one-dimensional tests proposed by TM97 and Ovtchinnikov and Easter (2009). Both use a constant wind (so the analytical solution is simply the translation of the initial condition) and consider two tracers that are related nonlinearly (TM97) and three tracers that add up to a constant (Ovtchinnikov and Easter 2009), respectively. None of these idealized multi-tracer tests have been extended to two dimensions or been applied in highly deformational/divergent flows, and the numerical mixing has not been systematically categorized nor quantified. The systematic and largely irreversible generation of small scales in tracer fields by the deformational nature of the flow is a ubiquitous feature of atmospheric transport, and is crucial for controlling mixing and other processes in the real atmosphere (Pierrehumbert 1991, 1995; Thuburn and Tan 1997; Balluch and Haynes 1997). We consider it crucial that any practical transport scheme should be tested on flow fields of realistic complexity, allowing assessment of the scheme's ability to handle the generation of small scales and the resulting numerical mixing.

Three test case setups designed to quantify numerical mixing for one, two and three tracers are proposed. For a single tracer the numerical mixing is quantified in terms of an entropy diagnostic. In the case of two tracers that are nonlinearly correlated, mixing diagnostics to quantify the mixing and to analyze how physically reasonable the numerical mixing is are presented. This provides indicators for excessive numerical mixing as well as unphysical numerical unmixing. For three tracers we consider the situation in which the three tracers add up to a constant. Ideally the sum should be preserved, however, most

shape-preserving transport operators will perturb the sum when transporting the tracers individually. We argue that the proposed mixing diagnostics are physically motivated metrics for the issues of interest; they complement the conventional error norms and may be more appropriate and useful when choosing a transport scheme for chemical-transport modelling.

Although these test cases do not require the knowledge of the analytical solution for the transport problem, we exercise the mixing diagnostics with a recently developed idealized flow field which is highly deformational (Nair and Lauritzen 2010, hereafter referred to as NL10) and where the analytical solution is known (at the end of the simulation). Using an analytical flow field and the fact that the true solution is known facilitates the application of the multi-tracer mixing diagnostics in transport scheme development and allows for the computation of conventional error norms alongside the new mixing diagnostics. The proposed test cases are illustrated using the cubed-sphere version of the CSLAM (Conservative Semi-LAgrangian Multi-tracer) scheme (Lauritzen *et al*. 2010). Obviously any global transport scheme on the sphere could be used for this demonstration.

The paper is organized as follows. In section 2 we introduce the transport equation and associated notation, discuss preexisting functional relations and define the new mixing diagnostics. The idealized test case setup using an analytical wind field and spatial distributions is described in section 3. Mixing diagnostics for the idealized test case suite using the CSLAM scheme are presented in section 4 followed by a discussion on the mixing diagnostics and their relevance to nonlinear chemistry parameterizations (section 5). Section 6 contains a discussion and conclusions.

2. Method

2.1. Continuous and discretized transport equations

Consider a transport scheme that approximates the solution to the continuity equation for an inert (no sources or sinks) and passive (tracer does not feed back on the flow) tracer,

$$\frac{\partial(\rho\phi)}{\partial t} + \nabla \cdot (\rho\phi\,\mathbf{V}) = 0, \quad \phi = \chi, \xi, \zeta \qquad (1)$$

where ρ is the air density, $\mathbf{V}$ is the flow velocity vector, and $\phi = \chi, \xi, \zeta$ is the tracer mixing ratio for the different interrelated tracers considered in this paper. The continuity equation (1) is written in flux-form; however, the transport scheme may be based on the continuity equation in another form (e.g., advective form). To 'extract' the mixing ratio ϕ from (1) obviously requires the solution to the continuity equation for air density ρ (see, e.g., NL10 for details). All analysis in this test case suite is based on mixing ratio ϕ and not tracer density $\rho\,\phi$.

Assume that the spatial domain is discretized with N points/cells so that each point/cell holds mixing ratios χ_k, ξ_k, and ζ_k, $k = 1, .., N$. The range of values taken by χ_k, $k = 1, .., N$ at the initial time is denoted $[\chi^{(min)}, \chi^{(max)}]$ and similarly for ξ_k and ζ_k.

Let $\mathcal{T}$ be the discrete transport operator that advances the numerical solution for ϕ at grid point k in time

$$\phi_k^{n+1} = \mathcal{T}(\phi_j^n), \quad j \in \mathcal{H}, \qquad (2)$$
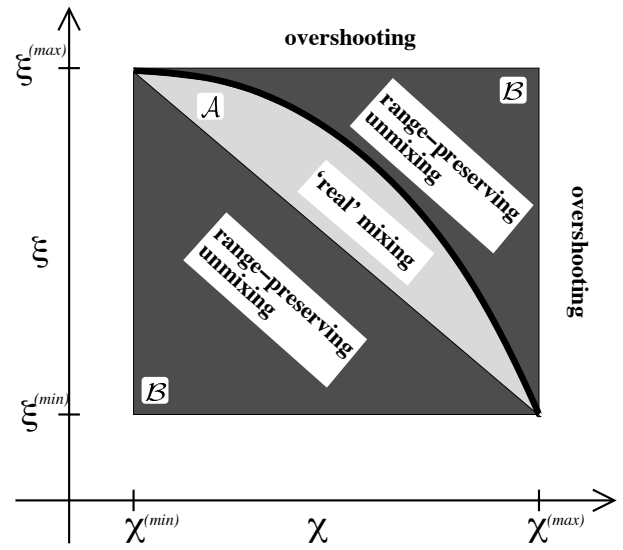

Figure 1. A schematic of the classification of numerical mixing. The thick solid line is the preexisting nonlinear functional curve $(\chi, \psi(\chi))$. For each grid point k the numerical transport scheme generates a point (χ_k, ξ_k) on the scatter plot. If (χ_k, ξ_k) is inside the 'convex hull' $\mathcal{A}$ (light-shaded area) the numerical mixing resembles *'real'* mixing in that scatter points are shifted to the concave side of $(\chi, \psi(\chi))$. Any scatter point outside $\mathcal{A}$ results in numerical unmixing that is classified into two categories. If (χ_k, ξ_k) is located to the convex side of ψ or below the convex hull but within the range of the initial data (dark-shaded areas denoted $\mathcal{B}$), the scheme produces umixing referred to as *range-preserving unmixing*. Scatter points in neither $\mathcal{A}$ nor $\mathcal{B}$ produce unmixing referred to as *overshooting*.

where n is the time-level index and $\mathcal{H}$ is the set of indices defining the stencil required by $\mathcal{T}$ to update ϕ_k. A solution to (2) requires an initial condition, a specified velocity field and may also require the solution to the continuity equation for air density ρ. In this paper the proposed test cases are two-dimensional and the diagnostics are described for the two-dimensional case; but note that the diagnostics generalize straightforwardly to the three-dimensional case.

2.2. Mixing for a single tracer

Before discussing mixing between tracers, it is interesting to note that single tracer mixing can be quantified using an entropy measure

$$S_\phi = -k_B \sum_{k=1}^{N} \phi_k \log \phi_k \, \rho_k \, \Delta A_k, \qquad (3)$$

where k_B is Boltzmann's constant and ΔA_k is the spherical area of grid cell k. For simplicity we assume a unit sphere (radius one) for the computation of S_ϕ.

If there are no numerical errors, the entropy is conserved in time. Exact conservation of entropy may be realized by a fully Lagrangian scheme that tracks Lagrangian areas through-out the integration. In that case, $\rho_k \Delta A_k$ is constant at all times for a given Lagrangian cell k moving with the flow (there is no flux of mass across the Lagrangian cell boundaries) and following fluid parcels ϕ_k is conserved indefinitely. For other kinds of schemes truncation errors will change the entropy. Real mixing can only increase the entropy, and S_ϕ is maximized (for a given total tracer mass) when ϕ is uniform. Typically, transport schemes tend to smooth gradients in ϕ and there will be a tendency for S_ϕ to increase due to numerical smoothing or

spreading and it will reach its maximum if the numerical diffusion reduces the distribution to a constant. However, we note also the possibility for a transport scheme to reduce entropy if dispersion errors lead to unmixing.

Define the entropy diagnostic as the relative change in entropy

$$\ell_s = \frac{S_\phi - S_\phi^{(init)}}{S_\phi^{(init)}}, \qquad (4)$$

where $S_\phi^{(init)}$ is the entropy of the initial condition. The diagnostic (3) requires knowledge of the density ρ as well as the tracer mixing ratio ϕ. The test case defined below uses a non-divergent flow field; therefore we propose to use the exact solution $\rho = 1$ for all t in computing this diagnostic, so that it is a measure only of how well ϕ is handled.

The entropy diagnostic has a number of limitations. First, as discussed above, a certain amount of numerical mixing is inevitable at finite resolution. It is therefore not immediately clear what constitutes a good result for the entropy diagnostic. To address this, we propose to compute a benchmark solution using a very high resolution solution coarse-grained to the test resolution; this benchmark gives an estimate of the best that could possibly be achieved at the test resolution. More details are given in section 4. Also, net change in entropy can result from a combination of local increases (mixing, diffusion) and decreases (unmixing, dispersion). Consequently there is the possibility of cancellation of errors and the entropy diagnostic may indicate favorable results for the wrong reasons. However, schemes with a shape-preserving filter will usually be dominated by real mixing rather than unmixing. Finally, if the transport scheme produces negative mixing ratios ℓ_s will no longer be well-defined. An advantage of the entropy diagnostic is that, contrary to standard error norms widely used for assessing truncation errors in idealized single-tracer test cases, it does not need the 'true' solution to the transport problem

2.3. Preexisting functional relation between two tracers

2.3.1. Linear correlations

A transport scheme will preserve linear correlations between two tracers if the transport operator $\mathcal{T}$ is *semi-linear*, that is,

$$\mathcal{T}(a\phi + b) = a\mathcal{T}(\phi) + b\mathcal{T}(1) = a\mathcal{T}(\phi) + b, \qquad (5)$$

for any constants a and b (Lin and Rood, 1996; TM97). Hence predicting two species χ and $\xi = a\chi + b$ independently will not disrupt the linear relation between the two. Finite-volume schemes are, in general, semi-linear if the reconstruction function they are based on is linear in the cell averaged values. For example, the widely used reconstruction method called the piecewise parabolic method (Colella and Woodward 1984) satisfies this constraint whereas the piecewise rational method (Xiao *et al.* 2002) does not. Some limiters/filters used to enforce shape-preservation render the scheme nonlinear but still semi-linear (e.g. Harris *et al.* 2011). While the preservation of linear correlations has received some attention in the literature and schemes have been designed to preserve linear functional relations between two tracers (e.g. Lin and Rood 1996), preservation of nonlinear functional relationships (or the lack thereof) has received little attention.

2.3.2. Nonlinear correlations

No practical Eulerian or semi-Lagrangian scheme will exactly preserve nonlinear preexisting functional relations and will therefore distort such relationships in some way. Suppose the mixing ratios of two tracers χ and ξ are initially related by $\xi = \psi(\chi)$. In principle any ψ that is a single-valued function in $[\chi^{(min)}, \chi^{(max)}]$ can be used. For the mixing diagnostics that are defined below it is convenient also to assume that the $(\chi, \psi(\chi))$-curve is only concave or only convex in $[\chi^{(min)}, \chi^{(max)}]$. If the transport operator $\mathcal{T}$ distorts the preexisting functional relationship, it essentially introduces numerical mixing or numerical spreading. How the scatter points deviate from $\psi(\chi)$ has consequences for the physical realizability of the numerically computed solution. Real mixing in the atmosphere can only move scatter points to the concave side of the preexisting functional curve ψ along mixing lines (e.g., TM97). More precisely, this area for which the numerical mixing resembles real mixing is the convex hull of the original scatter plot in the $\chi - \xi$ plane ($\mathcal{A}$ on Fig. 1). Any scatter point outside the convex hull corresponds to numerical unmixing and does not resemble real mixing. In many cases the most problematic unmixing occurs if the transport operator expands the range of the initial conditions for the tracers, which we refer to as *overshooting* (see Fig. 1). Overshooting may result in physically unrealizable mixing ratios, such as negative values, causing problems for sub-grid-scale parameterizations and chemistry schemes. If scatter points move to the convex side of the preexisting functional curve $\mathcal{T}$ produces spurious unmixing referred to as *range-preserving unmixing* ('upper' area $\mathcal{B}$ on Fig. 1). Scatter points within the range of the initial condition data but below the straight line connecting the end points of the pre-existing functional relation curve are also classified as range-preserving unmixing ('lower' triangular area $\mathcal{B}$ on Fig. 1).

TM97 showed that only schemes that are semi-linear and monotone[‡] as defined by Harten (1983) are guaranteed to produce numerical mixing only within the convex hull. Unfortunately only first-order schemes satisfy these constraints (Godunov 1959) and therefore some numerical unmixing must be accepted for most atmospheric applications as first-order schemes are considered too diffusive. Thus higher-order schemes that are shape-preserving and thus do not overshoot may produce range-preserving unmixing by shifting scatter points to the convex side of ψ or below the convex hull. Below we introduce mixing diagnostics that quantify numerical mixing in the three categories discussed above.

2.4. Mixing diagnostics for two nonlinearly correlated tracers

Assume that two tracers are related through a nonlinear preexisting functional relation ψ at the initial time so that

$$(\chi_k(t=0), \xi_k(t=0)) = (\chi_k, \psi(\chi_k)), \quad k = 1.., N, \qquad (6)$$

and that $\psi(\chi)$ is either concave or convex in $[\chi^{(min)}, \chi^{(max)}]$. As the mixing diagnostics are only based on deviations from the preexisting functional relation

---

[‡]Here 'monotone' means $\partial\phi_k^{n+1}/\partial\phi_j^n \geq 0$ for all k, j

they do not involve the analytical solution to the transport equation for the individual tracers.

2.4.1. Mixing that resembles 'real' mixing $\mathcal{A}$

This diagnostic accounts for numerical mixing that resembles 'real' mixing in that values are only shifted to the concave side of the preexisting functional relation within the convex hull (see Fig. 1)

$$\ell_r = \frac{1}{A} \sum_{k=1}^{N} \begin{cases} d_k \, \Delta A_k, & \text{if } (\chi_k, \xi_k) \in \mathcal{A}, \\ 0, & \text{else,} \end{cases} \quad (7)$$

where A is the total area of the domain, $A = \sum_{k=1}^{N} \Delta A_k$. The distance function d_k is the normalized shortest distance between the point (χ_k, ξ_k) and the $(\chi, \psi(\chi))$-curve where χ is constrained to the initial condition interval $\chi \in [\chi^{(min)}, \chi^{(max)}]$. For the quadratic functional relation ψ given in (21) with coefficients (22), the explicit formula for d_k is given in Appendix B. The domain $\mathcal{A}$ is the light-shaded area ('convex hull') on Fig. 1 that mathematically can be defined as

$$\mathcal{A} = \left\{ (\chi, \xi) \, \middle| \, \chi_k \in [\chi^{(min)}, \chi^{(max)}] \text{ and} \right.$$

$$\left. \mathcal{F}(\chi_k) \leq \xi_k \leq \psi(\chi_k) \right\}, \quad (8)$$

where $\mathcal{F}$ is the straight line that connects $(\chi^{(min)}, \xi^{(max)})$ and $(\chi^{(max)}, \xi^{(min)})$. Mixing that produces scatter points not in $\mathcal{A}$ is numerical unmixing that is accounted for in two distinct diagnostics.

2.4.2. 'Range-preserving' unmixing $\mathcal{B}$

This diagnostic accounts for numerical unmixing within the range of the initial data, that is, scatter points that are shifted to the convex side of the preexisting functional relation or below the convex hull but not outside the range of the initial data

$$\ell_u = \frac{1}{A} \sum_{k=1}^{N} \begin{cases} d_k \, \Delta A_k, & \text{if } (\chi_k, \xi_k) \in \mathcal{B}, \\ 0, & \text{else,} \end{cases} \quad (9)$$

where $\mathcal{B}$ is the dark-shaded area in Fig. 1 defined by

$$\mathcal{B} = \left\{ (\chi, \xi) \, \middle| \, (\chi_k, \xi_k) \in [\chi^{(min)}, \chi^{(max)}] \right.$$

$$\left. \times [\xi^{(min)}, \xi^{(max)}] \text{ and } (\chi_k, \xi_k) \notin \mathcal{A} \right\}, \quad (10)$$

The shape-preservation constraint is not necessarily enough to guarantee $\ell_u = 0$. As mentioned above, a scheme must be semi-linear and monotone as defined by Harten (1983) to guarantee $\ell_u = 0$ (TM97).

2.4.3. Overshooting

This diagnostic accounts for unmixing that is not accounted for in the ℓ_u diagnostic and is referred to as overshooting or range-expanding unmixing. It is defined as

$$\ell_o = \frac{1}{A} \sum_{k=1}^{N} \begin{cases} d_k \, \Delta A_k, & \text{if } (\chi_k, \xi_k) \notin (\mathcal{A} \cup \mathcal{B}), \\ 0, & \text{else.} \end{cases} \quad (11)$$

A scheme that is shape-preserving will result in $\ell_o = 0$.

It is noted that the diagnostics are 'mutually exclusive' in the sense that for a particular scatter point (χ_k, ξ_k) a non-zero value of the distance function d_k is added to only one of the diagnostic functions. Hence

$$\ell_r + \ell_o + \ell_u = \frac{1}{A} \sum_k d_k \, \Delta A_k. \quad (12)$$

In general it is desirable that ℓ_o is zero and that the amount of umixing, which has to be tolerated for higher-order schemes, is much less than the numerical mixing that resembles real mixing ($\ell_u \ll \ell_r$). It is not necessarily desirable that ℓ_r should be zero; as discussed in section 1, some numerical mixing is inevitable with an Eulerian transport scheme, reflecting the finite resolution of the grid. As with the entropy diagnostic, we define a benchmark solution that gives an estimate of the best ℓ_r achievable at a given test resolution. See section 4 for details.

2.5. Three or more tracers adding to a constant

As mentioned in the introduction multiple tracers may have a complicated relation to each other but they may add up to a constant or a smooth relation. A practical example is total reactive chlorine in the stratosphere. With just two tracers, preserving a constant sum reduces to preserving linear correlations; however, with more than two tracers it is, in general, more challenging for the scheme to preserve a constant sum. It is common practice in the modelling community that when the sum of tracers should be preserved the sum is also transported as a tracer, and then the individual tracers are adjusted to be consistent with the transported sum at every time-step (e.g. Douglass *et al.* 2004).

Here we consider three tracers that add up to a constant (for simplicity we assume that the constant is one)

$$\chi + \xi + \zeta = 1. \quad (13)$$

This relation should be preserved throughout the integration. If the transport operator is *linear* in the sense that

$$\mathcal{T}(\chi) + \mathcal{T}(\xi) + \mathcal{T}(\zeta) = \mathcal{T}(\chi + \xi + \zeta) = \mathcal{T}(1) = 1. \quad (14)$$

then it will preserve a constant sum. Note that this 'sum-requirement' (14) is not equivalent to the *semi-linear* property defined in (5). To quantify how nearly the scheme can preserve the constant by transporting the individual tracers χ, ξ, ζ, we use the standard error norms ℓ_1, ℓ_2 and ℓ_∞ for the difference between the sum $\chi + \xi + \zeta$ and the constant 1. As for the mixing diagnostics ℓ_r, ℓ_u and ℓ_o used for two nonlinearly correlated tracers, the three-tracer mixing diagnostics do not require knowledge of the analytical solution to the transport problem for the individual tracers.
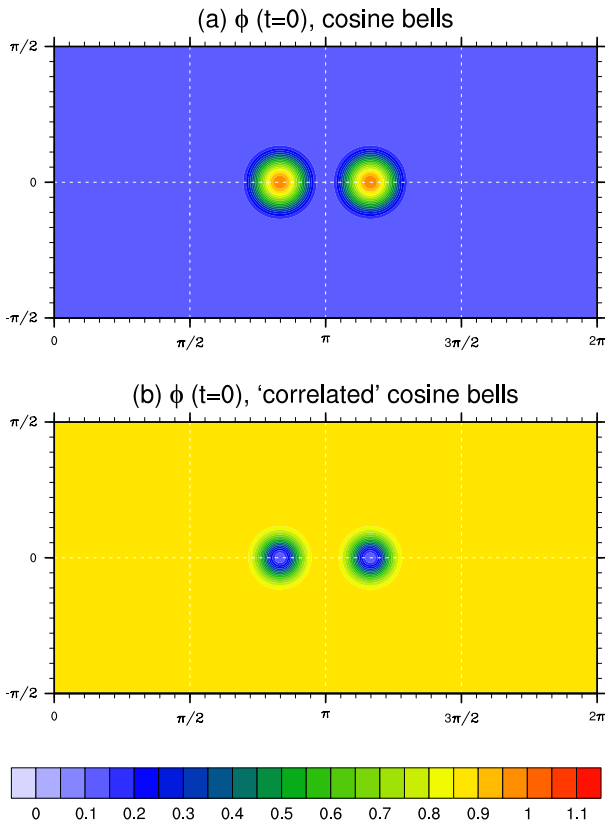
(a) ϕ (t=0), cosine bells

(b) ϕ (t=0), 'correlated' cosine bells

Figure 2. Contour plots of mixing ratio for the two correlated initial conditions. (a) depicts the cosine bells initial condition which is C^1 and (b) is the initial condition which is nonlinearly correlated with (a) according to ψ in (21).

3. Test case setup

3.1. Time-varying wind field

For the idealized test case setup we use a two-dimensional non-divergent wind field from NL10 which is highly deformational. The specific components of the velocity vector $\mathbf{V}(\lambda, \theta, t)$ and the stream function that we use here are given by (case 4 in NL10)

$$
\begin{align}
u(\lambda, \theta, t) &= \kappa \sin^2(\lambda') \sin(2\theta) \cos(\pi t/T), \quad (15) \\
&\quad + 2\pi \cos(\theta)/T \\
v(\lambda, \theta, t) &= \kappa \sin(2\lambda') \cos(\theta) \cos(\pi t/T), \quad (16) \\
\psi(\lambda, \theta, t) &= \kappa \sin^2(\lambda') \cos^2(\theta) \cos(\pi t/T) \quad (17) \\
&\quad - 2\pi \sin(\theta)/T,
\end{align}
$$

respectively, where λ is longitude, θ is latitude, $T = 5$, $\kappa = 2$, and $\lambda' = \lambda - 2\pi t/T$. The wind field is defined in non-dimensional units, however, the problem can easily be dimensionalized for Earth[*]. Schemes based on characteristics (typically Lagrangian schemes) may use the algorithm given in NL10 for the computation of parcel trajectories. Although we use a non-divergent wind field ((15) and (16)) to exercise the new mixing diagnostics in this paper, one may equally well use a divergent wind field (e.g., case 3 of NL10). In principle, any flow that develops

---

[*]e.g., $\kappa = 10\,r/T$ and the last term on the right-hand side of (15) should be $2\pi r \cos(\theta)/T$, where r is 6.3172×10^6 m and $T = 12$ days.

small-scale features in the tracer fields from larger-scale initial conditions should be appropriate.

Since Lagrangian parcels do not follow great-circle arcs the analytical solution at $t = T/2$ is not easily accessible. Therefore NL10 chose a time-reversing flow so that the deformed tracer fields at $t = T/2$ will return to their initial position and shape at $t = T$. To avoid the possibility of cancellation of errors when the flow reverses the deformational part of the flow is overlaid on a zonal background flow. The first half of the simulation $t \in [0, T/2]$, in which tracer features are collapsing to smaller scales, is typical of atmospheric flows. The second half $t \in [T/2, T]$, in which the reverse occurs, is atypical of atmospheric flows though very convenient for getting a problem with a known exact solution. Since the mixing diagnostics do not require an analytical solution and since the first half of the simulation is more realistic than the second half, we compute the mixing diagnostics half way through the simulation. The computation of standard error norms, which do require a 'true' solution, is performed at $t = T$.

3.2. Initial conditions for one- and two-tracer tests

Two symmetrically located cosine bells are defined as follows,

$$
h_i(\lambda, \theta) = \frac{h_{\max}}{2}[1 + \cos(\pi r_i/r)] \quad \text{if} \quad r_i < r, \quad (18)
$$

where $h_{\max} = 1$, $r = 1/2$ is the base radius of the bells, $r_i = r_i(\lambda, \theta)$ is the great-circle distance between (λ, θ) and a specified center (λ_i, θ_i) of the cosine bell

$$
r_i(\lambda, \theta) = \arccos[\sin\theta_i \sin\theta + \cos\theta_i \cos\theta \cos(\lambda - \lambda_i)].
$$

The initial condition $\phi^{(cb)}$ consists of a background value g and two cosine bells with centers (λ_i, θ_i), $i = 1, 2$, respectively, generated using (18)

$$
\phi^{(cb)}(\lambda, \theta) = \begin{cases} g + c\,h_1(\lambda, \theta) & \text{if } r_1 < r, \\ g + c\,h_2(\lambda, \theta) & \text{if } r_2 < r, \\ g & \text{otherwise,} \end{cases} \quad (19)
$$

where the parameters are $g = 1/10$ and $c = 9/10$ such that the values of $\phi \in [1/10, 1]$, $(\lambda_1, \theta_1) = (5\pi/6, 0)$ and $(\lambda_2, \theta_2) = (7\pi/6, 0)$ as in case 4 of NL10 (see Fig. 2a). The initial condition nonlinearly correlated with $\phi^{(cb)}$ is

$$
\phi^{(ccb)} = \psi\left(\phi^{(cb)}\right), \quad (20)
$$

where

$$
\psi(\chi) = a\,\chi^2 + b, \quad \chi \in [\chi^{(min)}, \chi^{(max)}] \quad (21)
$$

with coefficients

$$
a = -\frac{8}{10} \quad \text{and} \quad b = \frac{9}{10}, \quad (22)
$$

(Fig. 2b). Hence for the two-tracer test we use initial conditions $\chi = \phi^{(cb)}$ and $\xi = \phi^{(ccb)}$ for the first and second tracer, respectively.
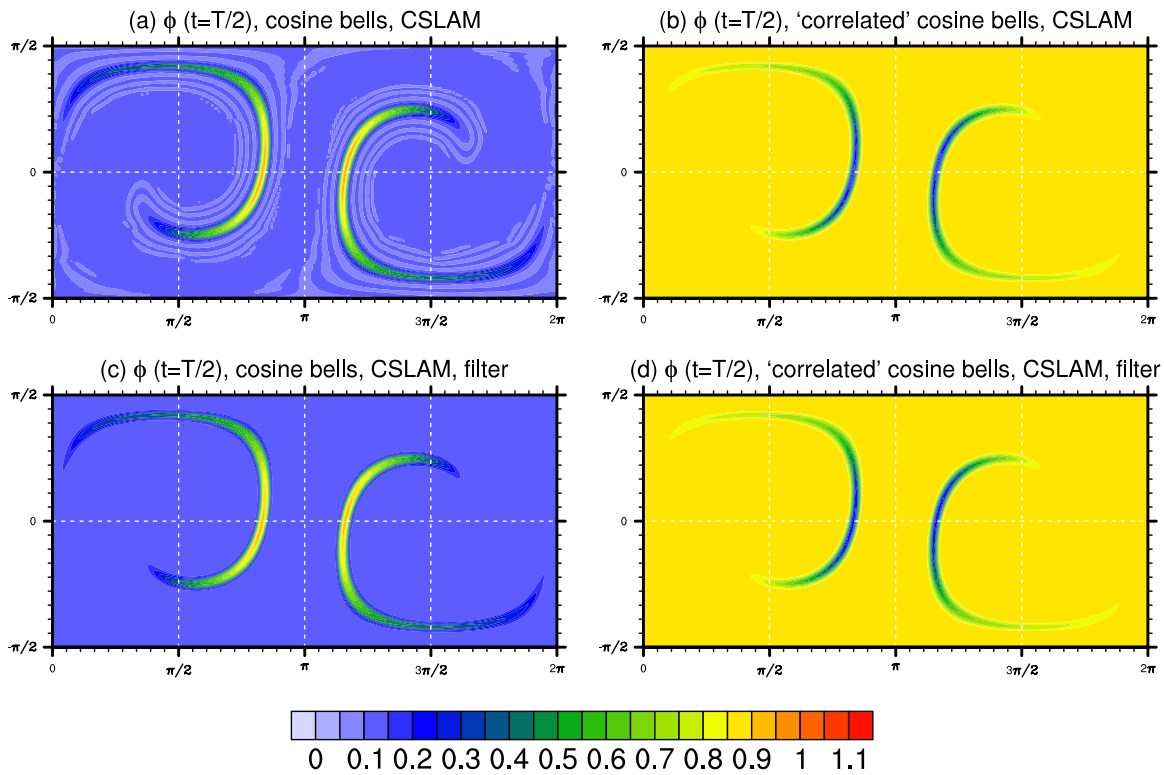
Figure 3. The numerical solution at $t = T/2$ for the cosine bells and correlated cosine bells initial conditions (first and second column, respectively) using CSLAM with and without a shape-preserving filter (first and second row, respectively).
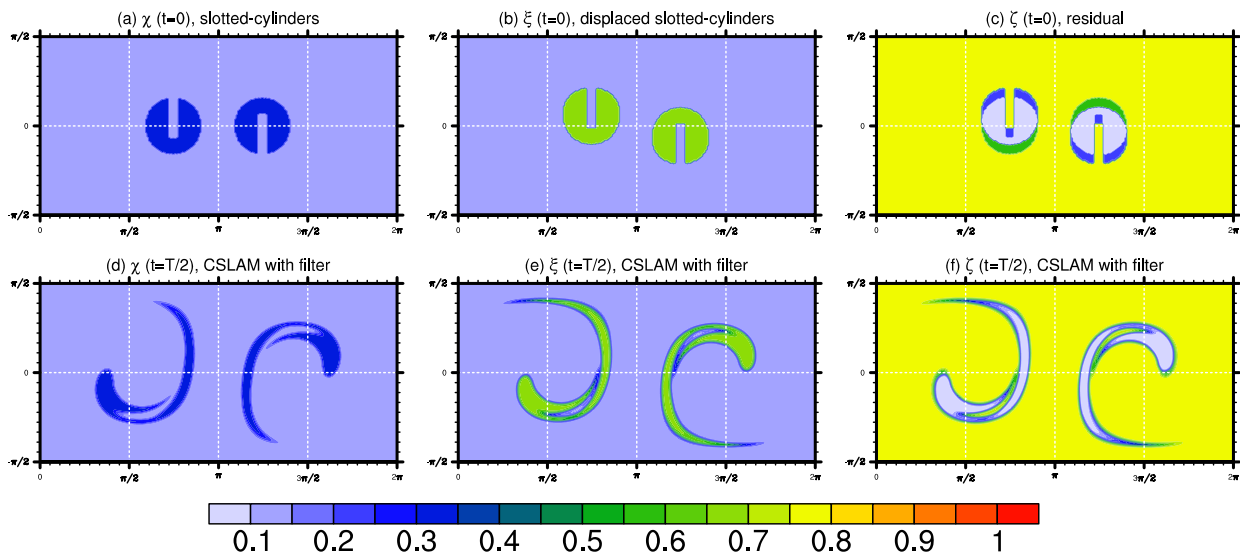

Figure 4. Contour plots of the slotted-cylinder initial conditions (a) $\chi(t = 0)$, (b) $\xi(t = 0)$ and (c) $\zeta(t = 0)$, respectively, and the corresponding shape-preserving CSLAM solutions at $t = T/2$ (d,e,f), respectively, for the three-tracer test.

3.3. Initial conditions for the three-tracer test

Following the one-dimensional three-tracer test proposed in Ovtchinnikov and Easter (2009) we use non-smooth initial conditions; this is most likely to activate shape-preserving filters in the transport scheme, and is relevant to the most challenging cases met in practice such as the steep chemical gradients seen near the terminator (e.g. Santillana *et al.*

2010). The double cosine-bells (19) are replaced by *slotted-cylinders* (Zalesak 1979) defined as follows,

$$\phi = \phi^{(sc)}(\lambda, \theta) = \begin{cases} c & \text{if } r_i \leq r \text{ and } |\lambda - \lambda_i| \geq r/6 \\ & \quad \text{for } i = 1, 2, \\ c & \text{if } r_1 \leq r \text{ and } |\lambda - \lambda_1| < r/6 \\ & \quad \text{and } \theta - \theta_1 < -\frac{5}{12}r, \\ c & \text{if } r_2 \leq r \text{ and } |\lambda - \lambda_2| < r/6 \\ & \quad \text{and } \theta - \theta_2 > \frac{5}{12}r, \\ g & \text{otherwise,} \end{cases}$$

(23)

where $r = 1/2$ for all tracers whereas constants c and g depend on the tracer. For the first tracer χ we choose initial condition $\phi^{(sc)}$ with $(\lambda_1, \theta_1) = (3\pi/4, 0), (\lambda_2, \theta_2) = (5\pi/4, 0)$, $c = 1/3$ and $g = 1/10$ (see Fig. 4a). Following Ovtchinnikov and Easter (2009) the initial condition for the second tracer ξ is displaced, in this case $10°$ in latitude, with respect to χ so that $(\lambda_1, \theta_1) = (3\pi/4, \pi/18), (\lambda_2, \theta_2) = (5\pi/4, -\pi/18)$ and the amplitude is different ($c = 2/3$) but the background value remains the same ($g = 1/10$) (Fig. 4b). The initial condition for the third tracer is the residual so that the tracers add up to one:

$$\zeta(t = 0) = 1 - [\chi(t = 0) + \xi(t = 0)], \qquad (24)$$

(see Fig. 4c).

4. Results

The proposed test cases are demonstrated using the CSLAM scheme (for a review of finite-volume schemes used in meteorology see, e.g., Machenhauer *et al.* 2009; Lauritzen *et al.* 2011). The coupling between the air density and tracer mixing ratio used in CSLAM is described in detail in Appendix B of NL10. Unless stated explicitly otherwise we use an equi-angular cubed-sphere grid with 60×60 cells per panel which corresponds to a $1.5°$ resolution at the Equator. The time-step used for the $1.5°$ resolution is $\Delta t = T/120$ which for the NL10 flow (their case 4) will result in a maximum CFL number in each coordinate direction locally on each panel of approximately 5.5. For shape-preservation the simple filter of Barth and Jespersen (1989) that scales the sub-grid scale reconstruction function so that its extrema do not exceed the cell-averages of the neighboring cells is used.

Fig. 3 shows the numerical solution half way through the simulation at $t = T/2$ with and without the shape-preserving filter (first and second row, respectively) for the $\phi^{(cb)}$ and $\phi^{(ccb)}$ initial conditions (first and second column, respectively). Similarly, Fig. 4d-f shows the numerical solutions for the three tracers in the three-tracer test at $t = T/2$ with the shape-preserving filter. The initial distribution is stretched into thin filaments half way through the simulation while being transported Eastward. This flow was designed to challenge the transport operator $\mathcal{T}$ by being highly deformational so that small-scale features develop from large-scale initial conditions and simultaneously the small-scale features must be translated over significant distances. For schemes defined on grids that have singularities away from the filaments that develop at $t = T/2$ modelers are encouraged to rotate the flow to direct the distributions over 'trouble' points.

Note also that the cosine bell shapes and slotted-cylinders are overlaid on a non-zero constant background value to challenge the shape-preservation operator so that simple negative filling algorithms will not alleviate oscillations near the base of the deformed fields (e.g., Fig. 3a).

4.1. Entropy diagnostic for a single tracer: CSLAM example

To exercise the entropy mixing diagnostic for a single tracer (3), we show time-traces of ℓ_s for different configurations of CSLAM on Fig. 5. The entropy diagnostic ℓ_s is a function of the air density ρ, the entropy of the initial condition, $S_\phi^{(init)}$,
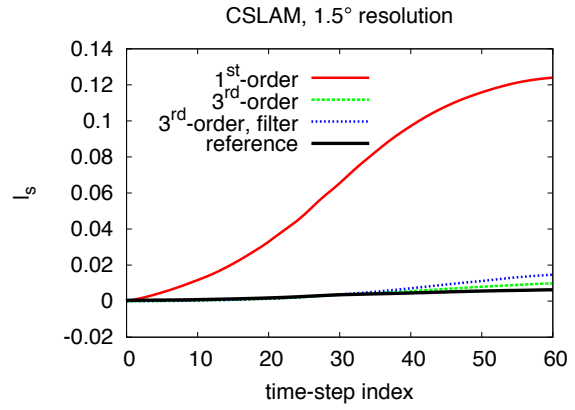

Figure 5. Entropy diagnostic ℓ_s (assuming a unit sphere) as a function of time-step index for different configurations of CSLAM at approximately $1.5°$ resolution (upper three lines) using the cosine bells initial condition $\chi = \phi^{(cb)}$. The thick solid black line is ℓ_s as a function of time-step index of the high resolution reference solution (approximately $0.09375°$) averaged to approximately $1.5°$.

and the mixing ratio ϕ. For simplicity and since the flow is non-divergent we assume the exact solution for air density: $\rho = 1$ for all t.

For the first half of the simulation, $t \in [0, T/2]$, shown on Fig. 5 the entropy increases with time due to numerical spreading of the solution. Not surprisingly the higher-order configuration of CSLAM produces much less mixing (much less increase in entropy) compared to the first-order version. Adding a shape-preserving filter increases the entropy due to additional numerical diffusion. The diagnostics in the next section suggest that it is not simply the case that the filtered version produces more mixing than the unfiltered version. In fact it produces less 'real' mixing, but also less unmixing; since unmixing is associated with a decrease in entropy, there are compensating effects associated with the two processes. For the change in entropy production compared to the unfiltered version, the decrease in unmixing is the dominant effect.

To obtain a benchmark value for ℓ_s higher resolution solutions have been computed and then averaged to the $1.5°$ reference resolution before the computation of ℓ_s. For example, the test case has been run at $0.75°$ so that four high resolution grid cells span exactly one grid cell at $1.5°$ resolution. The high resolution solution is averaged to $1.5°$ by summing the product between mixing ratio and the respective grid cell areas, and then dividing this sum by the area of the coarse grid cell. Similarly for resolutions $0.375°$, $0.1875°$ and $0.09375°$ for which 16, 64, and 256 high resolution grid cells respectively span exactly one coarse $1.5°$ grid cell. This averaging to the $1.5°$ reference resolution is here referred to as 'coarse-graining'. The results for ℓ_s using the native grid and coarse-grained solutions are shown in Table I. As expected ℓ_s decreases as the horizontal resolution increases and the coarse-grained solution converges to a benchmark value $\ell_s^{(b)} = 6.3 \times 10^{-3}$. This value $\ell_s^{(b)}$ indicates the lowest/best value of ℓ_s one can expect at the $1.5°$ reference resolution. A scheme is excessively diffusive/mixing if it produces an increase in entropy much greater than the benchmark entropy value

$$\ell_s \gg \ell_s^{(b)} = 6.3 \times 10^{-3}. \qquad (25)$$

Table I. Real mixing ℓ_r and entropy ℓ_s diagnostics for shape-preserving CSLAM (3rd-order) at resolutions $1.5°$ ($\Delta t = T/120$), $0.75°$ ($\Delta t = T/240$), $0.375°$ ($\Delta t = T/480$), $0.1875°$ ($\Delta t = T/960$), $0.09375°$ ($\Delta t = T/1920$) corresponding to $60{\times}60$, $120{\times}120$, $240{\times}240$, $480{\times}480$, and $960{\times}960$ cells per panel, respectively. 'coarse-grained' refers to the diagnostic computed using the solution for ϕ averaged to the $1.5°$ reference resolution.

resolution	ℓ_r on native grid	ℓ_r coarse-grained	ℓ_s on native grid	ℓ_s coarse-grained
$1.5°$	$6.28{\times}10^{-4}$	$6.28{\times}10^{-4}$	$1.47{\times}10^{-2}$	$1.47{\times}10^{-2}$
$0.75°$	$1.05{\times}10^{-4}$	$2.72{\times}10^{-4}$	$1.93{\times}10^{-3}$	$6.65{\times}10^{-3}$
$0.375°$	$1.82{\times}10^{-5}$	$2.43{\times}10^{-4}$	$3.98{\times}10^{-4}$	$6.29{\times}10^{-3}$
$0.1875°$	$3.95{\times}10^{-6}$	$2.42{\times}10^{-4}$	$9.56{\times}10^{-5}$	$6.29{\times}10^{-3}$
$0.09375°$	$9.37{\times}10^{-7}$	$2.42{\times}10^{-4}$	$2.36{\times}10^{-5}$	$6.30{\times}10^{-3}$

First-order CSLAM produces much greater entropy increase than the benchmark value ($\ell_s \gg \ell_s^{(b)}$), while third-order CSLAM produces approximately 2.3 times the entropy increase compared to the benchmark ($\ell_s \sim \ell_s^{(b)}$).

4.2. Mixing diagnostics for two nonlinearly related tracers: CSLAM example

The mixing diagnostics for two nonlinearly related tracers ℓ_r, ℓ_u, ℓ_o described in section 2.4 are computed half way through the simulation ($t = T/2$) for the cosine bells initial condition and correlated cosine bells initial condition $(\chi, \xi) = \left(\phi^{(cb)}, \psi(\phi^{(cb)})\right)$, respectively.

Fig 6 shows scatter plots for different configurations of CSLAM. The corresponding mixing diagnostics and standard error norms are in Table II. For the first-order version of CSLAM based on constant reconstruction functions, the excessive numerical diffusion tends to move scatter points toward the upper-left corner of the convex hull (Fig 6a). As predicted by theory (TM97) the first-order version of CSLAM produces no overshooting ($\ell_o = 0$) because the scheme is inherently shape-preserving, and produces no unmixing ($\ell_u = \ell_o = 0$) because the scheme is linear (hence semi-linear) and monotone. The third-order version of CSLAM visibly produces much less clustering of the scatter points away from ψ which is reflected in the approximately one order of magnitude lower real mixing diagnostic ℓ_r (Fig 6b). Since the scheme is not shape-preserving the range of the initial condition is expanded ($\ell_o \neq 0$; left of convex hull on Fig 6b) and some range-preserving unmixing is introduced ($\ell_u \neq 0$; some scatter points on the convex side of ψ in Fig 6b). By invoking the shape-preserving reconstruction function filter no overshooting takes place $\ell_o = 0$ and, perhaps surprisingly, the level of unmixing in terms of ℓ_u is less than half compared to the solution without a filter and the level of real mixing ℓ_r is reduced by almost 20%. This is in contrast the entropy diagnostic ℓ_s which implies more mixing for each individual tracer. Also the ratio between real mixing and range-preserving unmixing (ℓ_r/ℓ_u) is approximately 9.3 for the filtered version of CSLAM compared to approximately 4.8 for the non-filtered version. Hence more numerical mixing within the range of the initial conditions resembles real mixing than non-physical unmixing in the filtered version of CSLAM.

In all, the filtered version of third-order CSLAM is superior to the unfiltered version in terms of the mixing diagnostics ℓ_r, ℓ_u, and ℓ_o. This is in contrast to the standard/conventional single tracer error norms that are minimized for the unfiltered third-order CSLAM (Table II). In terms of physical realizability and the non-existence of spurious oscillations, however, only the third-order version of CSLAM with a filter (and the first-order version) are acceptable.

As for the entropy diagnostic one may ask: what is best we can hope to achieve at the (finite) test resolution of $1.5°$? An estimate for that is given in terms of high resolution reference solutions coarse-grained to the $1.5°$ test resolution. Table I lists ℓ_r computed on high resolution grids as well as those solutions coarse-grained to $1.5°$. As expected ℓ_r tends to zero when increasing the resolution and the coarse-grained solutions converge to a benchmark value

$$\ell_r^{(b)} = 2.4 \times 10^{-4}. \qquad (26)$$

If $\ell_r \gg \ell_r^{(b)}$ for a particular scheme at approximately $1.5°$ resolution the real mixing is most likely excessive.

4.3. Three tracers adding up to a constant: CSLAM example

To trigger shape-preserving filters (that may introduce non-linearities) in the transport operator we use discontinuous initial conditions (slotted-cylinders) for this test. As mentioned in section 3.3 the three initial conditions are designed so that the sum of the tracers equals a constant, $\chi + \xi + \zeta = 1$. Obviously their sum should be preserved throughout the simulation. How nearly the discrete scheme can preserve the constant by transporting the individual tracers is a measure of some aspect of the non-linearity of the scheme.

The CSLAM scheme exactly preserves the sum by transporting the individual tracers when using the unfiltered version where no shape-preserving filter is invoked (not shown). However, the unfiltered version of CSLAM produces unphysical distributions (overshoots and wiggles) so a shape-preserving filter is needed for any practical application of the scheme. The filter used in CSLAM renders the scheme nonlinear in the sense that the sum is not preserved by transporting the three tracers individually (Fig. 7). Although the solution to the transport problem for the individual tracers is shape-preserving, their sum is not. At $t = T/2$ the standard error norms for the sum (a derived quantity) are $\ell_1 = 0.0025$, $\ell_2 = 0.0079$ and $\ell_\infty = 0.0653$. The figure shows that the largest errors in the sum occur along the sharp edges of the deformed slotted cylinders, as might be expected.

5. Discussion: Mixing diagnostics and their relevance to nonlinear chemistry parameterizations

The purpose of the mixing diagnostics proposed here is to enable information from advection-only test cases to be
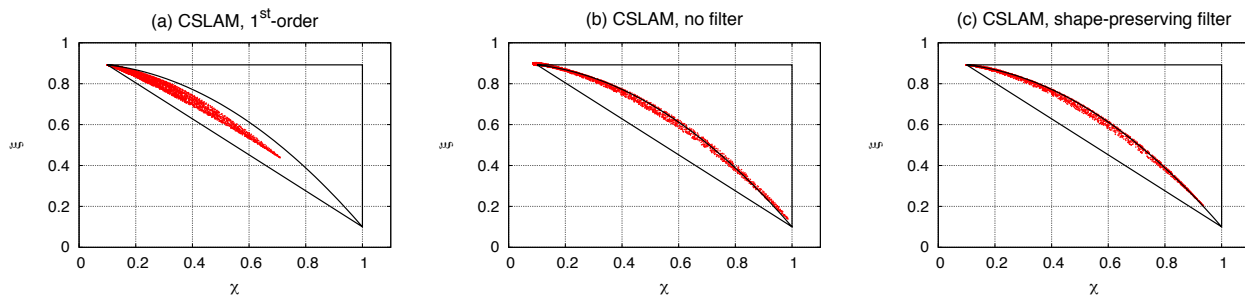
Figure 6. Scatter plots at $t = T/2$ for two nonlinearly correlated species based on cosine hills initial conditions using (a) first-order version of CSLAM, (b) standard CSLAM based on bi-parabolic reconstruction functions, and (c) standard CSLAM with a shape-preserving filter. The solid lines mark the boundaries between the areas used to classify the numerical mixing.

Table II. Columns 2,3 and 4 list standard error norms ℓ_1, ℓ_2 and ℓ_∞, respectively, at $t = T$ for a single tracer χ using initial condition $\phi^{(cb)}$ for different configurations of the CSLAM scheme. Second row is CSLAM based on constant reconstruction functions (1st-order), third row is third-order reconstruction functions and in the fourth row a shape-preserving filter has been applied to the third-order reconstruction function. The remaining columns (5,6,7) show mixing diagnostics ℓ_r, ℓ_u and ℓ_o at $t = T/2$ for the nonlinearly interrelated tracers χ and ξ initialized with $\chi = \phi^{(cb)}$ and $\xi = \psi\left(\phi^{(cb)}\right)$. Contour plots of the CSLAM numerical solution at $t = T/2$ for χ and ξ are on Fig. 3.

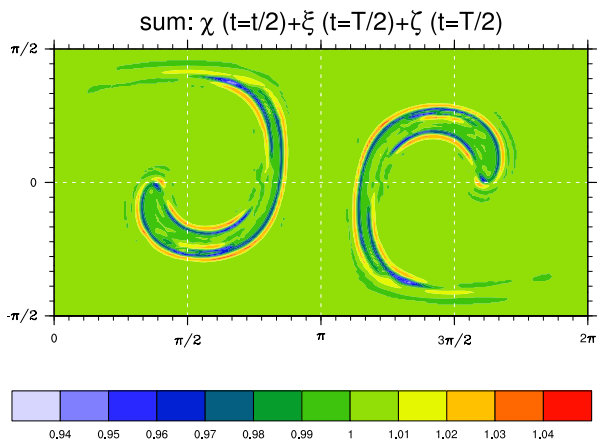| scheme	ℓ_1	ℓ_2	ℓ_∞	ℓ_r	ℓ_u	ℓ_o
1st-order CSLAM	1.93×10^{-1}	3.82×10^{-1}	4.57×10^{-1}	6.02×10^{-3}	0.0	0.0
3rd-order CSLAM	1.58×10^{-2}	3.28×10^{-2}	4.73×10^{-2}	7.55×10^{-4}	1.58×10^{-4}	3.79×10^{-4}
3rd-order CSLAM with filter	1.58×10^{-2}	4.33×10^{-2}	8.91×10^{-2}	6.28×10^{-4}	6.73×10^{-5}	0.0

Figure 7. Contour plot at $t = T/2$ for the sum of the individually transported tracers χ, ξ and ζ in the three-tracer test using the CSLAM scheme with a shape-preserving filter. Initial conditions for χ, ξ and ζ and CSLAM solution at $t = T/2$ are depicted on Fig. 4abc and Fig. 4def, respectively.

used to make predictions about the likely behaviour and possible problems when chemistry is included. To illustrate their usefulness, we consider an idealized but typical chemical reaction between two tracers with concentrations $(\chi - 0.1)$ and ξ, where χ and ξ are the solution fields in the two-tracer test. The reaction rate is assumed to be slow enough that we can neglect its effects on χ and ξ. We subtract the background value for χ so that the reaction rate is zero for the background distribution.

The rate at which product is formed at time t is proportional to the domain integrated reaction rate

$$R(t) = \sum_{k=1}^{N} (\chi_k - 0.1)\, \xi_k\, \Delta A_k. \tag{27}$$

For a non-divergent flow and in continuous space the instantaneous domain integrated reaction rate $\iint (\chi - 0.1)\,\xi\, dA$ is invariant in time.

The domain integrated reaction rate $R(t)$ may be partitioned into contributions from scatter points associated with 'real mixing' ($\mathcal{A}$), range-preserving unmixing ($\mathcal{B}$), and overshooting. Reaction rates associated with these three domains on the scatter plot are referred to as R_r, R_u and R_o, respectively. Obviously, $R = R_r + R_u + R_o$. Since numerical mixing is inevitable for practical semi-Lagrangian or Eulerian schemes the mixing introduced by the transport scheme should ideally manifest itself through 'real mixing' only and not unmixing. In terms of $R(t)$ the scheme providing the most physically realizable solutions should produce reaction rates dominated by R_r.

Results for reaction rates for different configurations of CSLAM are shown in Table III. Not surprisingly the first-order version of CSLAM overestimates the reaction rate at $t = T/2$ due to excessive numerical diffusion. The domain integrated reaction rate $R(t = T/2)$ for the non-shape-preserving version of third-order CSLAM is closer to the initial condition reaction rate than when applying a shape-preserving filter (similarly to what is observed for conventional error norms). However, the partitioning of the reaction rate into R_r, R_u, and R_o reveals that a larger fraction of the reaction rate is associated with 'real mixing' for the shape-preserving scheme than for the unlimited scheme. Moreover, R_u is less for the shape-preserving scheme than for the unlimited scheme. The reaction rate associated with overshooting in the unlimited scheme R_o is negative so for this particular reaction, R_o cancels errors in that it reduces the magnitude of $R(t = T/2)$ and thereby $R(t = T/2)$ is closer to $R(t = 0)$.

These results illustrate that even though the unlimited scheme is superior in terms of the total reaction rate $R(t = T/2)$, it is superior for unphysical reasons. The fraction of the reaction rate associated with unmixing fluid parcels

Copyright © 2011 Royal Meteorological Society

Prepared using qjrms4.cls

Q. J. R. Meteorol. Soc. **00**: 1–13 (2011)

Table III. Domain integrated reaction rates R at the initial time $t = 0$ (second column) and half time $t = T/2$ (third column) as well as the partitioning of the reaction rate at $t = T/2$ into parts associated with 'real' mixing (R_r), range-preserving unmixing (R_u) and overshooting (R_o; fourth, fifth and sixth column, respectively) for different configurations of the CSLAM scheme.

scheme	$R(t=0)$	$R(t=T/2)$	$R_r(t/T/2)$	$R_u(t/T/2)$	$R_o(t/T/2)$
1st-order CSLAM	$2.26{\times}10^{-1}$	$2.91{\times}10^{-1}$	$2.91{\times}10^{-1}$	0.0	0.0
3rd-order CSLAM	$2.26{\times}10^{-1}$	$2.30{\times}10^{-1}$	$1.59{\times}10^{-1}$	$7.25{\times}10^{-2}$	$-6.64{\times}10^{-4}$
3rd-order CSLAM with filter	$2.26{\times}10^{-1}$	$2.33{\times}10^{-1}$	$1.65{\times}10^{-1}$	$6.84{\times}10^{-2}$	0.0

is larger for the unlimited scheme than for the shape-preserving scheme. Similarly the reaction rate associated with 'real mixing' is larger for the shape-preserving scheme than for the unlimited scheme. The partitioning of $R(t)$ into R_r, R_u and R_o, and the differences between the partitioning for the three schemes, are consistent with the mixing diagnostics l_r, l_u and l_o for the three schemes. Hence the mixing diagnostics l_r, l_u, and l_o provide useful information on mixing-related chemical reaction rates and how physically realizable they are.

6. Summary and conclusions

In this paper we propose mixing diagnostics designed to assess how transport schemes introduce mixing and perturb preexisting functional relations between tracers. Three test cases based on one, two and three tracers as well as associated mixing diagnostics are proposed. Although the mixing diagnostics do not require knowledge of the true solution to the transport problem for each tracer, the mixing diagnostics are exercised using an idealized wind field (which is highly deformational) and for which the analytical solution exists at the end of the simulation.

The three idealized test cases are:

1. A single tracer χ initialized with the cosine bells initial condition is transported with the deformational flow that deforms the initial condition into thin filaments. Numerical mixing is quantified using an entropy diagnostic l_s.
2. Two tracers χ and ξ are nonlinearly related through a preexisting functional relation ψ. The initial condition for the first tracer is based on cosine bells and the second tracer is related to the first through a quadratic function. The numerical mixing is quantified in terms of the normalized distances of scatter points on a correlation plot from the preexisting functional relation curve. The mixing can be divided into mixing that resembles real mixing as observed in the atmosphere (ℓ_r; scatter points move along mixing lines) and spurious unmixing. The unmixing is split into unmixing that expands the range of the initial condition data (ℓ_o; overshooting) and mixing that moves scatter points to the convex side of the preexisting functional relation curve or below the convex hull (ℓ_u; range-preserving unmixing). Theoretically, overshooting can be controlled with shape-preserving filters ($\ell_o = 0$), but we cannot guarantee to avoid range-preserving unmixing ($\ell_u \neq 0$) for any scheme of higher than first order. Obviously it is desirable that the numerical mixing mostly resembles real mixing rather than spurious unmixing ($\ell_u \ll \ell_r$).
3. Three tracers χ, ξ, ζ, may have a complicated relationship among each other but add up to a constant ($\chi + \xi + \zeta = 1$). Obviously the constant is preserved in the exact case; however, schemes with shape-preserving filters will, in general, not be able to preserve the sum when transporting the tracers separately. The deviation of the sum from unity is quantified using standard error norms. To trigger nonlinearities in the transport scheme discontinuous initial conditions (slotted-cylinders) are used for this test case.

Example results using the CSLAM (Conservative Semi-LAgrangian Multi-tracer) scheme on the cubed-sphere are presented. Obviously any global transport scheme could have been used. It is shown that only first-order CSLAM will not produce unmixing ($\ell_u = \ell_o = 0$) and that a shape-preserving filter for the higher-order version of CSLAM will eliminate overshooting ($\ell_o = 0$) but not range-preserving unmixing ($\ell_u \neq 0$). Hence some unmixing must be tolerated if a higher-order scheme is used. Although the CSLAM scheme without filters performs better in terms of standard error norms, CSLAM with shape-preserving filters is superior in terms of the new mixing diagnostics.

For the particular test resolution used in this paper (approximately $1.5°$) we define benchmark values for the single-tracer entropy diagnostic ($\ell_s^{(b)}$) as well as two-tracer 'real mixing' diagnostic ($\ell_r^{(b)}$). This is done by computing very high resolution solutions coarse-grained to the test resolution; these benchmarks give estimates of the best that could possibly be achieved at the test resolution. If at approximately $1.5°$ resolution $\ell_s \gg \ell_s^{(b)}$ and $\ell_r \gg \ell_r^{(b)}$ for a particular scheme, the numerical spreading/mixing and real mixing, respectively, are most likely excessive. Mixing benchmark values can easily be estimated at other resolutions (if needed).

The usefulness of the proposed diagnostics is demonstrated by computing an idealized reaction rate between two transported species. The mixing diagnostics give useful predictive information about the overall reaction rate for different transport schemes, as well as the partitioning of that reaction rate into contributions associated with physically realizable 'real mixing' and unphysical unmixing and overshooting.

The proposed mixing diagnostics are physically motivated metrics designed to address issues of particular relevance to chemistry-transport modelling. They are intended to complement conventional error norms, not replace them. (For example, a scheme that simply preserves the initial data will produce favorable mixing diagnostics even though the solution is highly inaccurate.) Applying these diagnostics to state-of-the-art transport schemes could provide a point of comparison for the future development of new schemes (Lauritzen *et al.* 2011a,b). The proposed test case methodology provides a simple setup for assessing numerical mixing and it could potentially be used in the
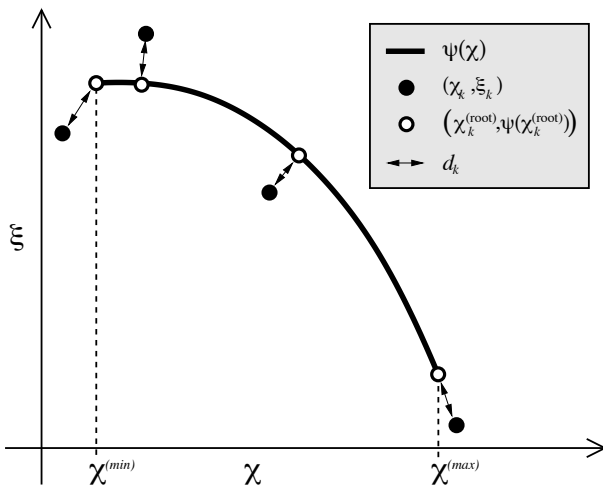
Figure 8. A schematic of d_k (left-right arrows) for different correlation points (χ_k, ξ_k) (filled circles) generated by the transport scheme. d_k is the 'normalized Euclidean distance' between (χ_k, ξ_k) and the point on the preexisting functional relation $(\chi, \psi(\chi))$ (thick line), where $\xi \in [\chi^{(min)}, \xi^{(min)}]$ (dashed lines), nearest to (χ_k, ξ_k). This nearest point on $(\chi, \psi(\chi))$ is denoted $(\chi_k^{(root)}, \psi(\chi_k^{(root)}))$ (unfilled circle).

development of better filters/limiters in terms of minimizing unphysical numerical mixing and producing mixing that resembles true mixing as observed in the atmosphere.

Acknowledgement

Appendix A: Conventional error norms

Conventional/standard errors norms for a numerically computed solution ϕ are given by

$$
\begin{aligned}
\ell_1 &= \frac{I(|\phi - \phi_T|)}{I(|\phi_T|)}, \\
\ell_2 &= \left[\frac{I[(\phi - \phi_T)^2]}{I[(\phi_T)^2]}\right]^{1/2}, \\
\ell_\infty &= \frac{\max_{\forall \lambda, \theta} |\phi - \phi_T|}{\max_{\forall \lambda, \theta} |\phi_T|},
\end{aligned}
$$

where ϕ_T is the analytical solution. The global integral I is defined as follows,

$$
I(\phi) = \frac{1}{4\pi} \int_0^{2\pi} \int_{-\pi/2}^{\pi/2} \phi(\lambda, \theta, t) \cos\theta \, d\lambda \, d\theta.
$$

Appendix B: Definition of distance measure d_k

For the mixing error norms the point on the $(\chi, \psi(\chi))$-curve closest to (χ_k, ξ_k) needs to be computed. Define the

function,

$$
L_k(\chi) = \sqrt{\left(\frac{\chi_k - \chi}{R_\chi}\right)^2 + \left(\frac{\xi_k - \psi(\chi)}{R_\xi}\right)^2}, \quad (28)
$$

where $\chi \in [\chi^{(min)}, \chi^{(max)}]$ and

$$
\begin{aligned}
R_\chi &= \chi^{(max)} - \chi^{(min)}, & (29) \\
R_\xi &= \xi^{(max)} - \xi^{(min)}, & (30)
\end{aligned}
$$

are the ranges of the initial data for χ and ξ, respectively. $L_k(\chi)$ is the normalized Euclidean distance between the correlation point (χ_k, ξ_k) and a point on the preexisting functional relation curve $(\chi, \psi(\chi))$. (We use the normalized distance so that, when a semi-linear transport scheme is used, the error norms are invariant when either tracer mixing ratio ϕ is replaced by $A\phi + B$ for constants A and B.)

The point $(\chi, \psi(\chi))$ that is nearest to (χ_k, ξ_k) is computed by solving

$$
\frac{d}{d\chi}[L_k(\chi)] = 0. \quad (31)
$$

For the specific coefficients ($a = -8/10$ and $b = 9/10$) and ranges (R_χ and R_ξ), the solution to (31) is given by

$$
\chi = \chi_k^{(root)} = c_k + \frac{1}{c_k}\left(\frac{13}{75} - \frac{5}{12}\xi_k\right), \quad (32)
$$

where

$$
c_k = \frac{1}{60}\left[65340\,\chi_k + 12\sqrt{12(125\,\xi_k - 52)^3 + 29648025\,\chi_k^2}\right]^{1/3}. \quad (33)
$$

The point $\left(\chi_k^{(root)}, \psi(\chi_k^{(root)})\right)$ is constrained to lie in $[\chi^{min}, \chi^{max}]$ since χ-values outside this interval are 'nonphysical'. Hence we define the minimum distance function d_k as

$$
d_k = L_k(\chi_k^{(\psi)}), \quad (34)
$$

where

$$
\chi_k^{(\psi)} = \min\left[\max\left(\chi^{(min)}, \chi_k^{(root)}\right), \chi^{(max)}\right]. \quad (35)
$$

References

Balluch MG, Haynes PH, 1997. Quantification of lower stratospheric mixing processes using aircraft data. *J. Geophys. Res.*, **102**, 487–23. doi:10.1029/97JD00607

Barth T and Jespersen D. 1989. The design and application of upwind schemes on unstructured meshes. *Proc. AIAA 27th Aerospace Sciences Meeting, Reno*

Colella P, Woodward PR. 1984. The Piecewise Parabolic Method (PPM) for gas-dynamical Simulations. *J. Comput. Phys.* **54**. 174–201

Doswell CA. 1984. A Kinematic Analysis of Frontogenesis Associated with a Nondivergent Vortex. *J. Atmos. Sci.* **41**: 1242–1248

Douglass AR, Stolarski RS, Strahan SE, Connell PS. 2004. Radicals and reservoirs in the GMI chemistry and transport model: Comparison to measurements, *J. Geophys. Res.*, **109**, D16302, DOI:10.1029/2004JD004632

Godunov SK. 1959. A difference scheme for numerical computation of discontinuous solutions of equations in fluid dynamics (in Russian). *Math. Sb.* **47**: 271

Harris LM, Lauritzen PH, Mittal R. 2011. A Flux-form version of the conservative semi-Lagrangian multi-tracer transport scheme (CSLAM) on the cubed sphere grid. *J. Comput. Phys.* **230**: 1215–1237. DOI:10.1016/j.jcp.2010.11.001

Harten A. 1983. On the symmetric form of systems of conservation laws with entropy. *J. Comput. Phys.* **135**: 260–278

Lauritzen PH, et al. 2011. A standard test case suite for 2D linear transport on the sphere: results from 17 state-of-the-art schemes. *Geoscientific Model Development*: in prep.

Lauritzen PH, Skamarock WC, Prather MJ, Taylor MA. 2011. A standard test case suite for 2D linear transport on the sphere. *J. Comput. Phys.*: in prep.

Lauritzen PH, Nair RD, Ullrich PA. 2010. A conservative semi-Lagrangian multi-tracer transport scheme (CSLAM) on the cubed-sphere grid. *J. Comput. Phys.* **229**: 1401–1424: DOI: 10.1016/j.jcp.2009.10.036

Lauritzen PH, Ullrich PA, Nair RD. 2011. Atmospheric transport schemes: Desirable properties and a semi-Lagrangian view on finite-volume discretizations. *Lecture Notes in Computational Science and Engineering* **80**. Springer.

Lin SJ, Rood RB. 1996. Multidimensional flux-form semi-Lagrangian transport schemes. *Mon. Wea. Rev.* **124**: 2046–2070

Machenhauer B, Kaas E, Lauritzen PH. 2009. Finite Volume Methods in Meteorology. *Handbook of Numerical Analysis,*. **14**: 3–120. Elsevier.

Nair RD, Jablonowski C. 2008. Moving Vortices on the Sphere: A Test Case for Horizontal Advection Problems. *Mon. Wea. Rev.* **136**: 699–711

Nair RD, Lauritzen PH. 2010. A Class of Deformational Flow Test Cases for Linear Transport Problems on the Sphere. *J. Comput. Phys.* **229**: 8868–8887, doi:10.1016/j.jcp.2010.08.014

Ovtchinnikov M, Easter RC. 2009. Nonlinear Advection Algorithms Applied to Interrelated Tracers: Errors and Implications for Modeling Aerosol-Cloud Interactions. *Mon. Wea. Rev.* **137**: 632-644

Pierrehumbert RT, 1991. Chaotic mixing of tracer and vorticity by modulated travelling Rossby waves. *Geophys. Astrophys. Fluid Dynamics*, **58**, 285-319.

Pierrehumbert RT, 1995. Tracer microstructure in the large eddy dominated regime. in *Chaos Applied to Fluid Mixing*, Ed. H.Aref, M.S., El Naschie, pp 347–365, Pergamon, Tarrytown, N.Y.

Plumb RA. 2007. Tracer interrelationships in the stratosphere. *Rev. Geophys.* **45**: RG4005, doi:10.1029/2005RG000179

Proffitt MH, Margitan JJ, Kelly KK, Loewenstein M, Podolske JR, Chan KR, 1990. Ozone loss in the Arctic polar vortex inferred from high-altitude aircraft measurements. *Nature* **347**: 31–36

Santillana M, LeSager P, Jacob DJ, Brenner MP, 2010. An adaptive reduction algorithm for efficient chemical calculations in global atmospheric chemistry models. *Atmospheric Environment* **44**: 4426–4431, doi: 10.1016/j.atmosenv.2010.07.044

Thuburn J, McIntyre ME. 1997. Numerical advection schemes, cross-isentropic random walks, and correlations between chemical species. *J. Geophys. Res.* **120(D6)**: 6775–6797

Thuburn J, Tan DGH. 1997. A parameterization of mixdown time for atmospheric chemicals. *J. Geophys. Res.* **102**: 13037–13049

Williamson DL, Drake JB, Hack JJ, Jakob R, Swarztrauber PN. 1992. A Standard Test Set for Numerical Approximations to the Shallow Water Equations in Spherical Geometry. *J. Comput. Phys.* **102**: 211–224

Zalesak ST. 1979. Fully multidimensional flux-corrected transport algorithms for fluids. *J. Comput. Phys.* **31**: 335–362

Xiao F, Yabe T, Peng X, Kobayashi H. 2002. Conservative and oscillation-less atmospheric transport schemes based on rational functions. *J. Geophys. Res.* **107**: 4609. DOI:10.1029/2001JD001532.